ISPRS Annals of the Photogrammetry, Remote Sensing and Spatial Information Sciences, Volume X-M-2-2025
30th CIPA Symposium “Heritage Conservation from Bits:
From Digital Documentation to Data-driven Heritage Conservation”, 25–29 August 2025, Seoul, Republic of Korea

Learning Anomalies to Highlight Archaeological Structures in Cluttered 3D Point Clouds: Demonstration on Terrestrial Scans of Desert Kites

Reuma Arav[1]

[1] Institute of Geomatics, Dept. of Ecosystem Management, Climate, and Biodiversity, BOKU University, 1190, Vienna, Austria - reuma.arav@boku.ac.at

Keywords: Saliency, Cultural Heritage, LiDAR, Convolution Neural Network (CNN), Machine-learning.

Abstract

Three-dimensional point clouds are becoming indispensable in archaeological studies. They are mostly used to document the site, to digitally visualize it, or to analyse its topographical context. Since many of the sites are embedded or semi-embedded within the terrain, they tend to be overlooked, misrepresented, or simply removed in the digital terrain modelling process. Therefore, a common practice is to manually mark them within the raw dataset and to add them to the finalized m odel. Here we propose a machine-learning approach to highlight regions that include archaeological features within 3D point clouds. It is based on the assumption that such features will present an anomaly within the surface. Therefore, the proposed method learns to reconstruct the surface from the acquired point cloud and then compares the reconstructed surface to the original one. In this way, a large error will signify an anomaly, i.e., a feature of interest within the point cloud. We demonstrate the proposed method on terrestrial laser scans of desert kites. These large ancient desert traps are found across the Middle-East and Central Asian arid and semi-arid regions. Their unique construction, made of two low long walls that converge into an enclosure, makes it difficult to distinguish them terrestrially. We show that using the proposed method, we can highlight the kites within the raw point cloud, without the need of an expert input and without labelled information.

1. Introduction

The utilisation of 3D point clouds for archaeology grows exponentially over the last two decades (Vinci et al., 2024). These point clouds are mostly used to document the archaeological site, to enhance its visualization, and to put it into topographical context (Cohen et al., 2020; Vinci et al., 2024; Sylaiou et al., 2025). Many of the documented sites are either embedded or partially embedded within the topography, i.e., they are to some degree part of the ground (Štular et al., 2021; Vinci et al., 2024). As a consequence, these sites are either wrongly classified as terrain, filtered out from the digital terrain model (DTM), or are simply misrepresented (Štular et al., 2021). Overcoming this, most applications manually detect the archaeological features and add them to the DTM (Lozić and Štular, 2021).

Recently, more and more studies aim to automate the identification archaeological features within 3D point clouds. These are usually applied on DTMs that were generated from the point clouds. For example, Risbøl et al. (2023) inspected a series of maps created from post-processing procedures over the DTM to highlight remnants of coastal dwellings. Analyses such as analytical hillshading, sky-view factor, openness, or local dominance were used for the task. Automating the detection, Toumazet et al. (2017) proposed a semi-automatic approach for the detection of grazing structures (“tras”). First, an archaeologist identifies one representative structure in the DTM. Then, potential structures in the data are found based on their morphology (e.g., have hollow parts). Lastly, a cross-correlation is estimated between candidates and the extracted representative. Lately, Wang et al. (2024) proposed a deep learning approach to detect old city walls that are partially embedded within the topography. Based on expert’s labelling of the DTM the authors trained a network to identify the location of the walls. Nonetheless, these methods still require expert input in order to provide good results. Therefore, they are site/feature specific and can hardly be generalized to other settings. Moreover, as the analyses are DTM-based, they are carried out on data which are reduced both in dimensionality (3D to 2.5D) and quality (i.e., interpolated data).

In this paper we propose an anomaly-based method to highlight embedded and partially embedded archaeological features in 3D point clouds. The proposed approach is driven by the fact that such features present an anomaly within the generally continuous and smooth landscapes. Therefore, we use a deep neural network to predict small parts of the landscape. The deviation between the actual and the predicted surface is interpreted as a measure of saliency/anomaly for that area. In this way, the proposed method is unlimited to specific objects or forms, nor to specific topographic settings. We demonstrate the proposed method to highlight desert kites in two different sites. These kites are large ancient stone constructions, presumably made for animal hunting or domestication purposes (Crassard et al., 2022; Nazari, 2024). They are characterized by long low walls and an enclosure (aka. head), both correspond to the topography (Arav et al., 2015). As such, they are embedded within the terrain and are difficult to distinguish. We show that the proposed method, applied directly to the raw point clouds, requires no expert intervention, is almost completely automatic, and is able to highlight both kites and other important environmental features.

2. Methodology

We seek to highlight archaeological features in point clouds, focusing on those that are embedded or semi-embedded within natural environments. Assuming that such features stand out

from their local surroundings, we define them as "salient regions", i.e., conspicuous areas in the data. Hence, we can use saliency detection methods to highlight archaeological features.

Works that aim to highlight salient regions in 3D point clouds are scarce. Handcrafted works usually search for an abrupt change in normal and/or curvature within a local neighbourhood (Ding et al., 2019; Hao et al., 2019; Arav and Filin, 2020; Arvanitis et al., 2022). In such schemes, there is a higher sensitivity to local variations, and hence to noise and rugged surfaces, which are common in open archaeological settings. Machine-learning based approaches mostly use pre-trained models, normally on small objects, where salient regions are labelled in advance (Zheng et al., 2019; Jiang et al., 2023). Here we use the approach proposed by Arav et al. (2025). In this method, neither labelling nor other external input are required. Moreover, it is fairly robust to measurement noise. In the following, we describe the principles of the method.

2.1 Saliency estimation in 3D point clouds by anomaly detection

To evaluate the reconstruction error as a saliency score, we use a 3D convolutional neural network (CNN) to reconstruct the surroundings of all points based on minimal information. When the surroundings are regular, the network will be able to reconstruct the surface with low reconstruction error. In cases where a feature of interest exists the surroundings will be irregular. Then, the network will be unable to reconstruct the surface and will yield a high reconstruction error.

As minimal information, we use a "shell" of a point's neighbourhood. The size of the neighbourhood (n) is defined by the user, according to the approximate minimal size of the features of interest. The shell (S_i for point i) is defined as the outer ring of the neighbourhood. The thickness of the shell (m) is predetermined by the user.

Training. Randomly selected points and their corresponding shells are automatically chosen from the point cloud. These are used to train the reconstruction network R. The network's parameters are obtained by minimizing the reconstruction error $\mathcal{R}(\hat{V}_i, V_i)$, with $\hat{V}_i$ and V_i the predicted and measured inner part of the shell, respectively. This approach has a major advantage, as it does not require any manually generated reference sets to train R. It should be mentioned that as the network is trained to reconstruct 'regular' surfaces and in each scene this 'regularity' might be different. Therefore, training has to be conducted for scenes with different terrain characteristics.

Reconstruction and reconstruction error. The network R predicts the values of $\hat{V}_i$ based on the shell S_i. Then, the error, interpreted as the saliency score ξ_i, is estimated by

$$\xi_i = \mathcal{R}(\hat{V}_i, V_i). \tag{1}$$

Validation and fine-tuning of the network. To stop the training process and to fine-tune the hyper-parameters, we use two subsets of the point cloud. One is composed of points that are expected to have high saliency scores (H), and another composed of points that are expected to have lower scores (L). Using these subsets, a saliency ratio $\hat{r}$ is defined:

$$\hat{r} = \frac{\bar{\xi}_H}{\bar{\xi}_L}, \tag{2}$$

with $\bar{\xi}_H$ the mean saliency score for points with a high expected saliency scores and $\bar{\xi}_L$ the mean saliency score for those with a low expected saliency. Ratios that are larger than 1 suggest that the mean estimated saliency scores in H is higher than those in L, which is the expected result. As these ratios approach 1, the distinction between the two regions decreases. When the ratio is smaller than 1, the prediction still requires more training, as regions that are expected to be with lower values yielded higher ones, and vice versa.

2.2 Implementation

We use the open-source implementation of Arav and Wittich (2023). There, the point cloud is represented by a voxel grid. Thus, the neighbourhood of a point p_i is of size $n \times n \times n$, such that V_i is centred at p_i. Only voxels with more than 2 points are considered as non-empty voxels and are used for training.

The shell thickness (m) is defined by the number of voxels that compose the shell. Therefore, its actual size also depends on the voxel size used to voxelize the point cloud.

The capacity of the network is parametrized by the parameter f, which describes the number of feature maps in base resolution.

2.3 Quality assessment

Measuring the performance of saliency scores is difficult. This is because the success rate cannot be easily quantified and may depend on user's understanding of the data (Vinci et al., 2016). Here we use saliency ratio for quantitative evaluation, which was suggested in Arav et al. (2025). Additionally, we visually inspect the results.

Using the saliency ratio defined in Eq. 2, we choose a different group of subsets H and L. Using this group, the saliency ratio is estimated so that ratios larger than 1 represent a good outcome of the proposed method, whereas those smaller than 1, suggest low performance. This is because as regions that should have been with higher scores received relatively low ones, and vice versa.

3. Study sites

Desert kites (aka. 'kites') are large stone constructions made of two long low walls. These walls ('arms'), which can be several kilometres long, converge into an enclosure ('head') (Barge et al., 2022; Crassard et al., 2022; Nadel et al., 2024; Nazari, 2024). Such kites are found across the Middle Eastern and Central Asian arid and semi-arid margins at different distributions (Abu-Azizeh et al., 2021; Barge et al., 2023). Defining the variability and structure of these desert kites help to better understand their functionality from the Neolithic to sub-contemporaneous times.

Despite their massive size, they are hardly visible from the ground (see Fig. 1a and Fig. 2a as examples). Therefore, most of desert kites documentation is carried out using satellite images, where specific construction details (e.g., stone size and arrangement or specific topographical settings) are left unrepresented.

In this paper, we focus on two kites in Southern Israel: Samar East (SE) and Pitam (PIT) (for specific locations see Nadel et al., 2010). One lies in a relatively planer area and the other are

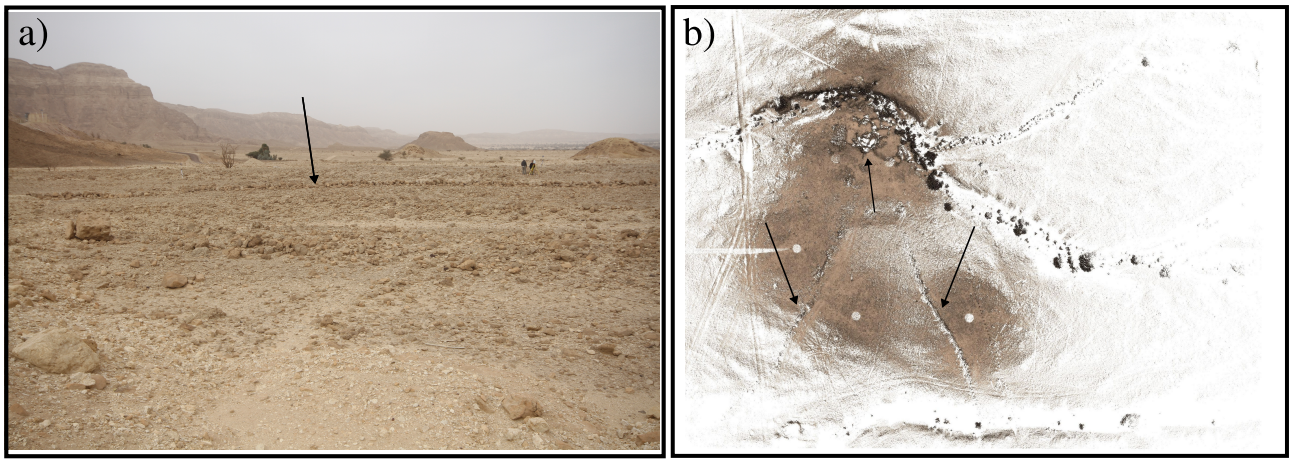

Figure 1. SE site. (a) Picture of one of the kite’s arms, with a guiding arrow (credit: Dani Nadel); (b) the acquired point cloud. White circles are scanning positions. The arrows point to the arms and head of the kite.

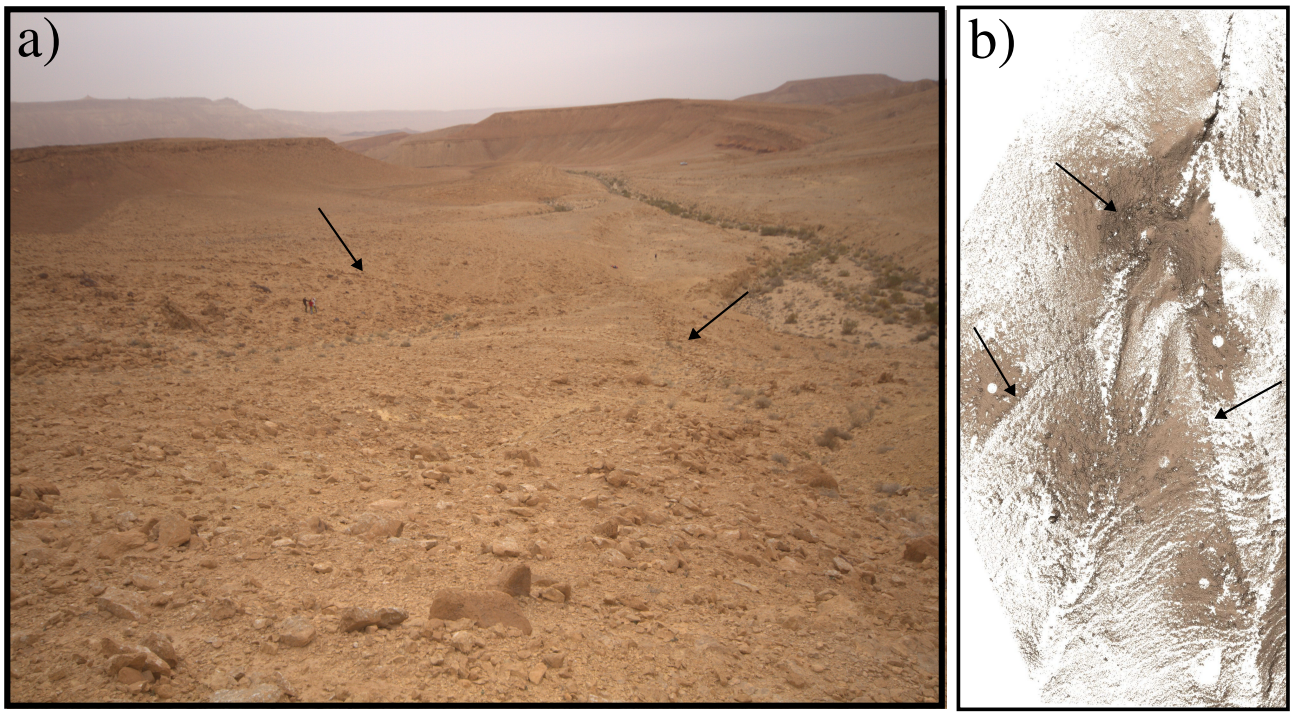

Figure 2. PIT site. (a) The kite’s arms (marked with a arrows; credit: Dani Nadel); (b) the acquired point cloud. White circles are scanning positions. The arrows point to the arms and head of the kite.

in a hilly region. The kites were documented during a terrestrial laser scanning campaign carried out in 2014 with a Leica Scanstation C10 (Arav et al., 2015). Scanning characteristics for both sites are summarized in Table 1.

3.1 Samar East kite (SE)

SE lies in a relatively flat area with low desert vegetation (Fig. 1a). The kite’s arms are 114 m and 137 m long (left and right in Fig. 1b, respectively), but parts closer to the head are missing. The wall of the right arm is about 0.3 m high, but can be as low as 0.1 m or as high as 0.5 m in some parts. The left arm has suffered more damages and therefore less continuous. Its height varies between 0.1 m-0.2 m. The head is partly preserved to its original height of 1.2 m. It lies on the edge of a small wadi (ravine) in which desert vegetation grows.

The site was scanned from six positions: five along the arms and one within the head (Fig. 1b and Table 1).

3.2 Pitam kite (PIT)

The Pitam kite lies in a hilly terrain of hard limestone with little vegetation (Fig. 2a). The kite’s arms are 77 m and 97 m long (left and right in Fig. 2b, respectively). The right arm descends along a steep slope, while the left begins on a plateau, crosses a narrow rugged wadi, and then turns sharply (almost by 90°) into the head. Both arms height varies between 0.12 m to 0.3 m. An excavation at the head revealed that a rampart and not a wall was built around the head to capture the animals (Arav et al., 2015; Nadel et al., 2021).

Eight positions were used to scan this kite, one of them within the head and the rest along the arms (Fig. 2b and Table 1)

Site	Type	No. of points [Millions]	Point density [pts/m^2]	Area [m^2]	No. of scan positions
SE	Planar	11.601	270	150×210	6
PIT	Hilly	15.125	300	500×300	8

Table 1. Scanning characteristics of the study sites.

4. Results and Discussion

We test the applicability of the proposed method to highlight the kites' features in the acquired terrestrial scans. We identify four important hyper-parameters: the number of features in base layer (f), the number of voxels in the voxel grid size (n), the voxel size, and the number of voxels in the grid shell (m). In both sites, 9 salient (H) and 9 non-salient (L) subsets were manually extracted. Of these, 6 were used for training and 3 for testing.

To choose f and n, we follow Arav et al. (2025) and run a set of experiments with a different number of features in base layer ($f = 16$, and 32) and at different voxel grid sizes ($n = 8, 24$, and 32). In these experiments, m is fixed to 3 voxels and the voxel size to 0.1 m, which is the approximate average point spacing in both datasets.

4.1 SE kite

Table 2 shows the average saliency ratio each combination of voxel/feature number has yielded for SE site. It can be seen that for all combinations, saliency scores are higher than 1. This implies that saliency scores evaluated by the proposed method are indeed higher where expected. The highest ratio, i.e., the combination that yielded the largest difference between salient and non-salient, was with 16 features in base layer and 32 voxels in the voxel grid.

Using this combination ($f = 16$, $n = 32$), we evaluated the saliency score for each point (Fig. 3). First, it can be seen that areas with lower point density received higher saliency scores. As the surface in these areas could not be reconstructed (too little points), the reconstruction error was high, leading to high saliency scores.

Within the region of interest, which was scanned at higher resolution, it can be seen that the right arm has yielded high saliency scores (Fig. 3a and (d)), as well as the head (a, b). Vegetation, rocks, and topographical variations are also marked with slightly higher saliency values (Fig. 3b). These do not exceed the score of 0.5. When comparing the saliency scores of the arms, it can be noticed that the left one is of lower scores (around 0.4 in some parts, compared to 1 in the right arm; Fig. 3a). This is probably due to the fact that the left arm is lower in height compared to the right arm (average of 0.15 m vs. 0.30 m, respectively). Indeed, in areas where the left arm is higher, a saliency score of 1 was received (Fig. 3 (a) and (d)). This is an expected result, as it shows that as the signature of the entity in the point cloud is stronger, the certainty of its identification is higher.

Some linear elements are highlighted with a score of approx. 0.4 (see examples marked with magenta arrows in Fig. 3a and (c)). These are possibly pathways that are used by current herds to cross the kite (Nadel et al., 2021). Note that such pathways are unnoticeable by simple visual examination of the raw point cloud.

n \ f	16	32
16	1.31±0.04	1.31±0.01
24	2.16±0.02	2.16±0.02
32	**2.61±0.01**	2.48±0.02
32	3.16 ±0.01	Voxel size 1 m
32	3.01 ±0.01	$m = 6$

Table 2. Saliency ratio (average and standard deviation over 2 runs, a-dimensional) in SE at voxel size 0.1 m and shell width of 3 voxels. The last two rows show the saliency ratio for voxel size 1 m and shell width of 6, respectively. f is the number of features in base layer and n is the voxel grid size length, represented by the number of voxels.

n \ f	16	32
16	1.36±0.02	1.36±0.01
24	1.55±0.01	1.56±0.01
32	**1.70±0.01**	1.68±0.02
32	3.01 ±0.02	$m = 6$

Table 3. Saliency ratio (average and standard deviation over 2 runs, a-dimensional) in PIT at voxel size 0.1 m and shell width of 3 voxels. The last row shows the saliency ratio for shell width of 6. f is the number of features in base layer and n is the voxel grid size length, represented by the number of voxels.

Fig. (4) shows saliency scores that were evaluated using $f = 16$ and $n = 32$, but with different voxel size (a) and shell width (b). It can be seen that when a larger voxel size was used for the analysis, a similar image is received (Fig. 4a). This is despite the higher saliency ratio (3.16; Table 2) that was achieved.

When a larger shell width was chosen ($m = 6$), a saliency ratio of 3.03 was obtained. This value is only slightly different from the one with 1 m voxel size (Table 2). Fig. (4b) shows that the saliency scores in this configuration were overall lower. Still, relatively speaking, the same image was obtained: the same regions are highlighted or marked non-salient (Fig. 4). This shows that in this case, even though the network managed to reconstruct the surface better, its ability to identify embedded entities does not increase.

4.2 PIT kite

The average saliency ratio each combination of voxel/feature number yielded for the PIT kite scan is shown in Table 3. Similar to the results in SE, saliency ratios are higher than 1 and the highest ratio was achieved for $f = 16$ and $n = 32$. However, the ratio values in this dataset are much lower. Also, the difference between the configurations is less distinguishable.

As the relatively low saliency ratio suggests, the network was able to reconstruct the surface only to a limited extent. The saliency scores evaluated for each point were in most regions larger than 0.5 (Fig. 5a). Higher saliency scores were given to areas with lower point density, similar to the effect seen in SE.

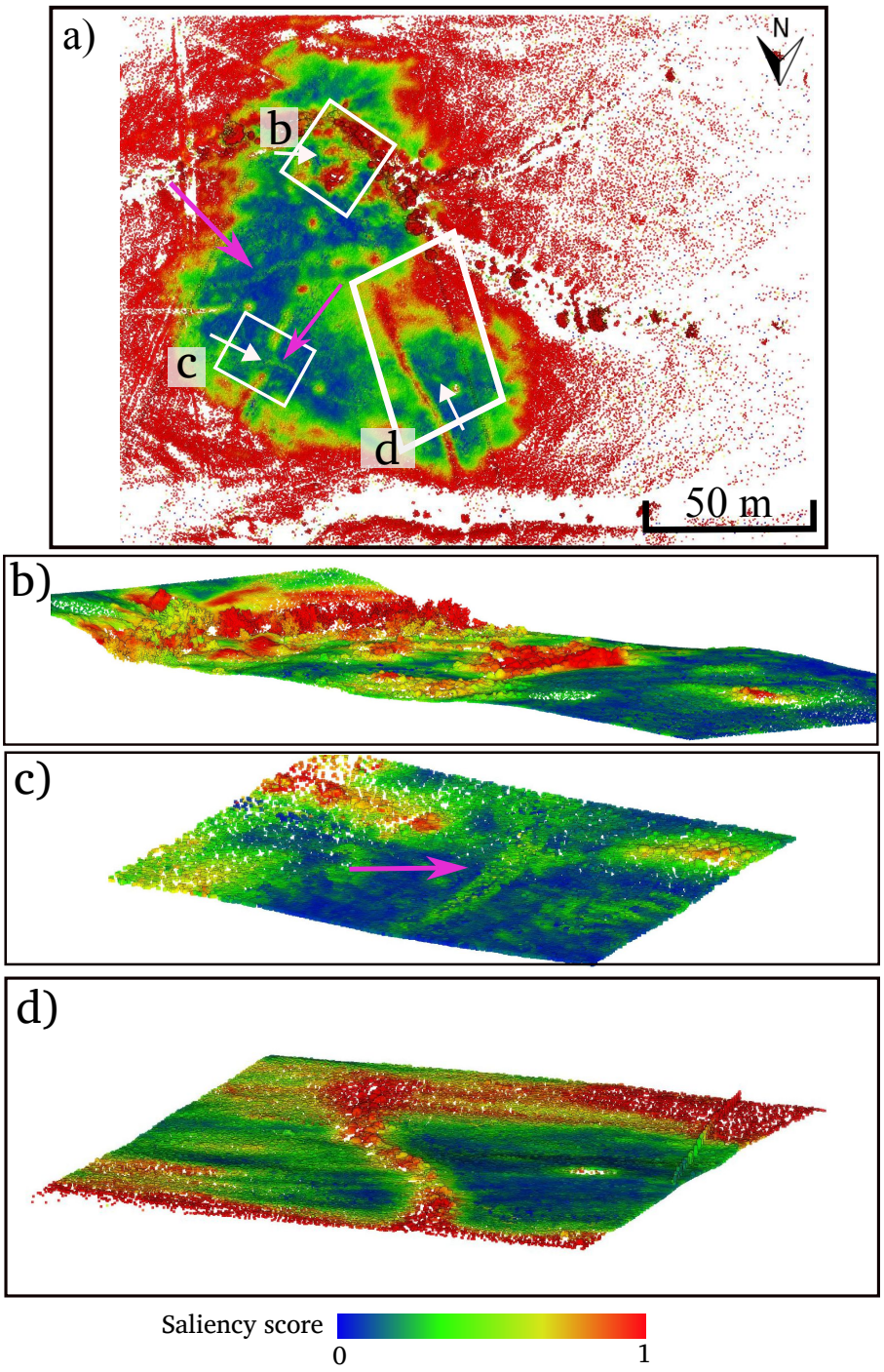

Figure 3. Estimated saliency scores for SE point cloud using $f = 16$, $n = 32$ and shell size of 3 voxels and voxel size of 0.1 m. The white arrows point to the approximate direction of each of the zoomed-in regions. (a) An overview of the entire SE point cloud and the evaluated saliency scores; (b) zoom-in on the head and the highlighted features within it; (c) zoom-in on the left arm of the kite: higher walls received saliency scores close to 1 (left), while the others yielded 0.5-0.7. A pathway (marked with magenta arrow) is slightly highlighted between the walls; (d) zoom-in on the highlighted right arm of the kite.

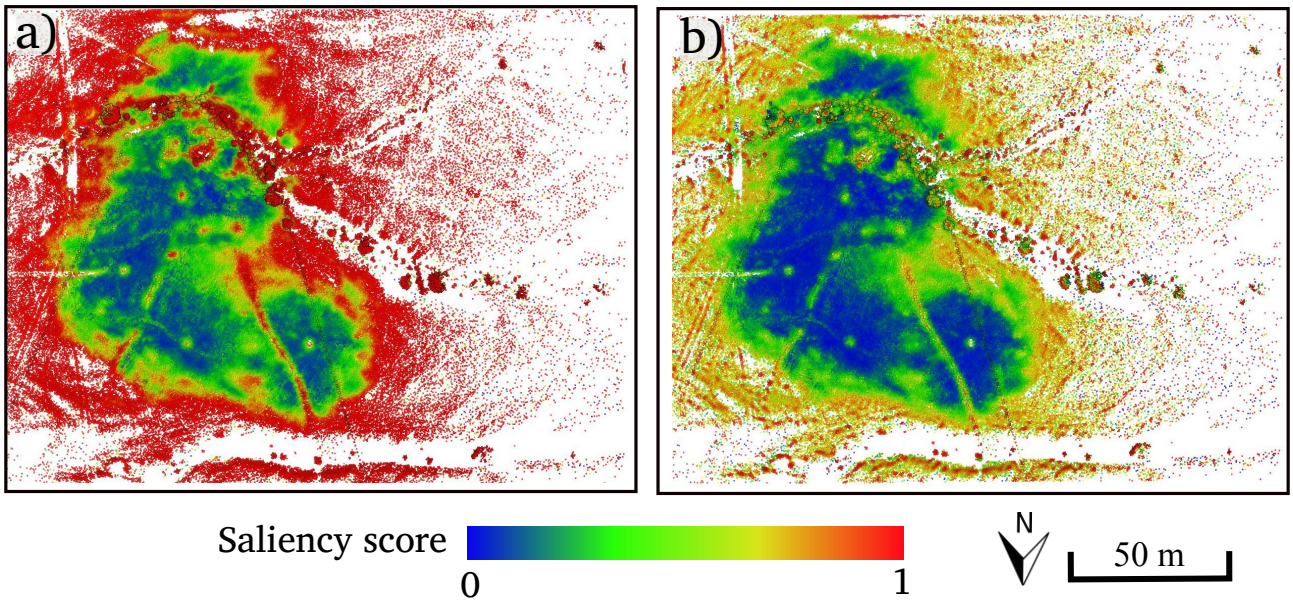

Figure 4. Estimated saliency scores in of SE using $f = 16$, $n = 32$ and (a) shell size of 3 voxels and voxel size of 1 m; (b) shell size of 6 voxels and voxel size of 0.1 m.

Since the entire dataset was given higher scores, it was difficult to visually inspect the results. To improve the visualization, points that have less than 20 neighbours in a 0.2 m radius were removed (Fig. 5b). This process revealed the kite’s arms, which were estimated with high saliency scores of approx. 1. Vegetation and large rocks also obtained such high saliency scores (see example in the orange rectangle in Fig. 5b) as well as the wadis that were scanned (e.g., the one between the arms, Fig. 5a).

The head also received high saliency scores (Fig. 5c). Here, the top stones in the construction were given scores that are close to 1, while the lower part yielded scores of approx. 0.5.

Using a shell width of 6 should provide more information for the network to learn how to reconstruct the surface. Therefore, we assume that it will improve the performance of the method in highlighting the kite’s features. We re-train the network with the configuration of $f = 16$, $n = 32$ and $m = 6$ (voxel size stays 0.1 m, per the results of SE). Using this configuration, a higher saliency ratio of 2.01 was achieved (Table 3), as expected. Fig. (6) shows the saliency score evaluated for each point in this case. It can be seen that the surface was indeed better reconstructed. The low point-density regions yielded saliency scores of up to 0.5, but not more. Unlike the case with $m = 3$, some regions were given scores of 0. Still, the kite’s features are not specifically highlighted. Instead, rocks and vegetation are marked with scores of approx. 1. This is probably due to the fact that this kite is completely embedded within the topography and has a subtle signature in the point cloud (Fig. 2a).

5. Conclusions

This paper presented an unsupervised method to highlight embedded and semi-embedded archaeological entities within terrestrial 3D point clouds. Based on the assumption that such entities will standout from their surroundings, we evaluate saliency scores as means for their identification. In this way, high saliency scores are assigned to points that are most likely to represent archaeological features. To do so, a network is trained to reconstruct the surface from as little information as possible. The surface is then reconstructed and compared to the scan. Higher saliency scores are given to regions that deviate from the expected reconstructed surface.

Two point clouds of desert kites were used to test the method’s applicability for archaeological purposes. The first kite has walls of up to 0.4 m and lies in a flat terrain. The other lies in a rocky, hilly, terrain with most walls not higher than 0.3 m. The first kite represented a semi-embedded entity whereas the second represented an embedded one. Both datasets were composed of several scanning positions, so that point density was changing drastically throughout the data.

In both sites, the combination of grid size with 32 voxels and 16 features in base layer yielded the highest saliency ratio. Enlarging either the shell width or the voxel size resulted in better surface reconstruction (i.e., higher saliency ratio). This is probably because more information was used to learn the surface. However, these higher ratios did not translate to better identification of the archaeological entities.

The proposed method was found sensitive to high point density variations. This is due to the amount of information used for the network to learn the reconstruction. In regions with low point density, the number of points in the shell was insufficient for the reconstruction. On the other hand, at high density regions, the number of points within the same shell size was sufficiently informative. The removal of low-density areas from the point cloud provided improved results, where the kite’s features were revealed. Nonetheless features such as vegetation and channels were given high saliency values (e.g., Fig. 3) while other archaeological features were given lower saliency values (e.g., the head in PIT, Fig. 5). Such shortcomings should be further looked into. As an example, an approach that adapts to point-resolution may solve false-positive detections.

Despite the complex settings in which the kites lie, the proposed method was able to identify them to some extent. Not only that, but it was also able to highlight important environmental features (like the pathways in SE) that are unidentifiable otherwise. By giving such features medium-range scores, a measure of uncertainty can be derived.

This contribution has been peer-reviewed. The double-blind peer-review was conducted on the basis of the full paper.
https://doi.org/10.5194/isprs-annals-X-M-2-2025-13-2025 | © Author(s) 2025. CC BY 4.0 License.

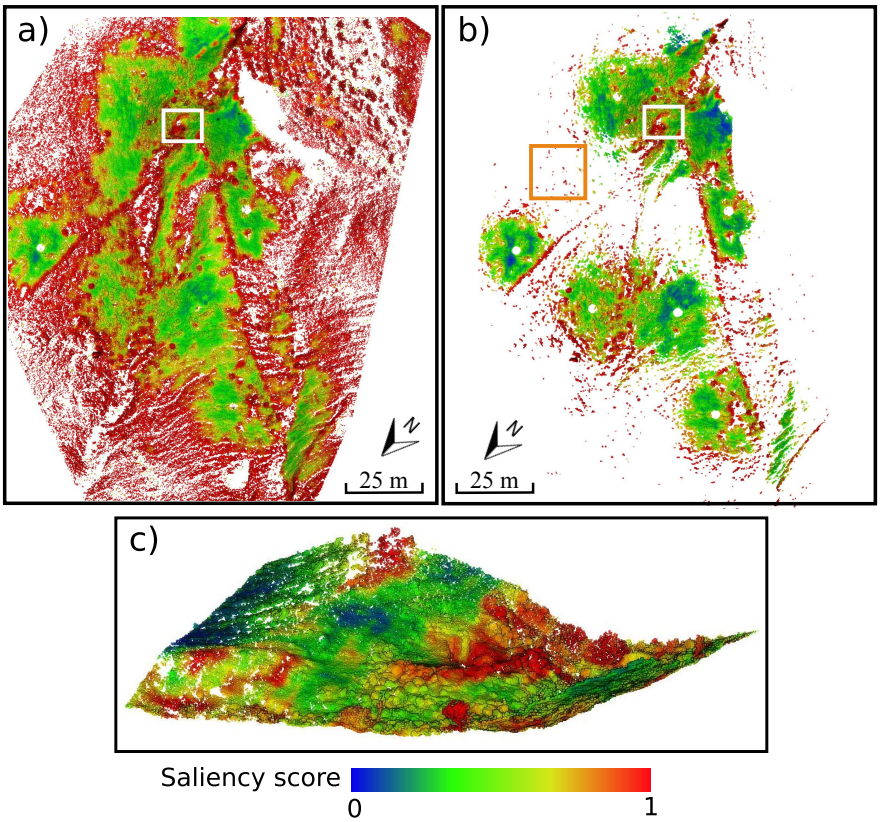

Figure 5. Estimated saliency scores for PIT point cloud using $f = 16$, $n = 32$ and shell size of 3 voxels and voxel size of 0.1 m.: a) for the entire point cloud. The white rectangle encompasses the head area; b) excluding points with lower density (less than 20 points in a 0.2 m radius). The orange rectangle is an example for larger rocks in the vicinity. c) zoom in on the head

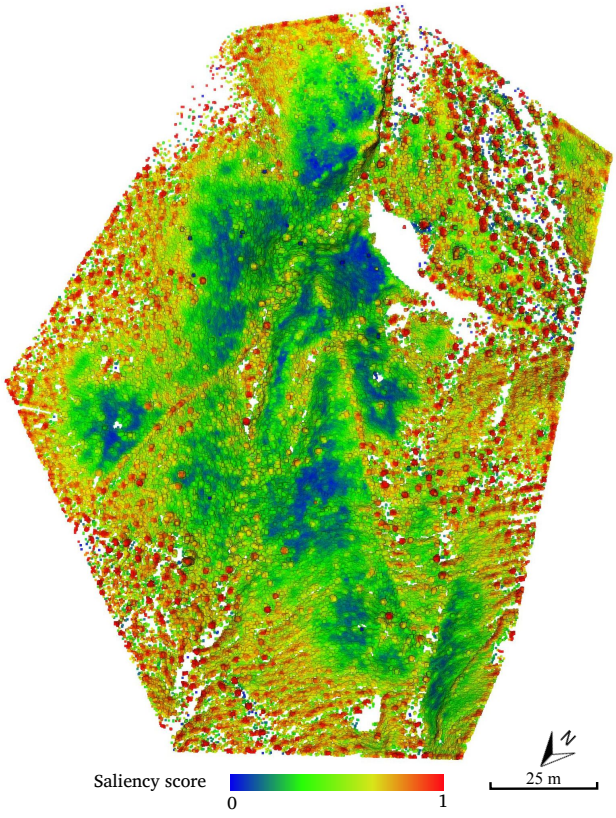

Figure 6. Estimated saliency scores in of PIT using $f = 16$, $n = 32$, a shell size of $m = 6$ and voxel size of 0.1 m.

The proposed method is data-driven and does not target specific entities or environment. Moreover, it does not require neither external information nor labelling. This method is therefore a first step towards the automatization of 3D identification of subtle archaeological entities in complex environment.

Acknowledgements

This work was supported in part by the European Union’s Horizon 2020 Research and Innovation Programme under the Marie Sklodowska-Curie Grant 896409. The author would also like to thank Prof. Franz Rottensteiner and Dr. Dennis Wittich for their contribution to the development of the method, Prof. Sagi Filin for sharing the data, and Prof. Dani Nadel for sharing the pictures.

References

Abu-Azizeh, W., Tarawneh, M., Crassard, R., Priego, J. A. S., 2021. *Discovery and excavation of desert kites in the south-eastern Badia of Jordan*. Sydney University Press, 225–252.

Arav, R., Filin, S., 2020. Saliency of subtle entities within 3-D point clouds. V-2-2020, Copernicus GmbH, 179–186.

Arav, R., Filin, S., Avner, U., Bar-Oz, G., Nachmias, A., Malkinson, D., Nadel, D., 2015. High-resolution documentation, 3-D modeling and analysis of “desert kites”. *Journal of Archaeological Science*, 57, 302–314.

Arav, R., Wittich, D., 2023. Salient ánomaly. *GitHub*. `https://github.com/rarav/salient_anomaly/releases/tag/v1.0.0`. last accessed: January 2025.

Arav, R., Wittich, D., Rottensteiner, F., 2025. Evaluating saliency scores in point clouds of natural environments by learning surface anomalies. *ISPRS Journal of Photogrammetry and Remote Sensing*.

Arvanitis, G., Zacharaki, E. I., Vasa, L., Moustakas, K., 2022. Broad-to-Narrow Registration and Identification of 3D Objects in Partially Scanned and Cluttered Point Clouds. *IEEE Transactions on Multimedia*, 24, 2230–2245.

Barge, O., Albukaai, D., Boelke, M., Guadagnini, K., Régagnon, E., Crassard, R., 2022. New Arabian desert kites and potential proto-kites extend the global distribution of hunting mega-traps. *Journal of Archaeological Science: Reports*, 42, 103403.

Barge, O., Bouzid, S., Abu-Azizeh, W., Régagnon, E., Crassard, R., 2023. Morphological and geographical variability of desert kites. *Archaeological and Anthropological Sciences*, 15(3).

Cohen, A., Klassen, S., Evans, D., 2020. Ethics in Archaeological Lidar. *Journal of Computer Applications in Archaeology*, 3(1), 76–91.

Crassard, R., Abu-Azizeh, W., Barge, O., Brochier, J. E., Chahoud, J., Régagnon, E., 2022. The Use of Desert Kites as Hunting Mega-Traps: Functional Evidence and Potential Impacts on Socioeconomic and Ecological Spheres. *Journal of World Prehistory*, 35(1), 1–44.

Ding, X., Lin, W., Chen, Z., Zhang, X., 2019. Point Cloud Saliency Detection by Local and Global Feature Fusion. *IEEE Transactions on Image Processing*, 1–1.

Hao, W., Liang, W., Wang, Y., Zhao, M., Li, Y., 2019. Saliency-Guided Repetition Detection From Facade Point Clouds. *IEEE Access*, 7, 150072–150081.

Jiang, Z., Ding, L., Tam, G. K., Song, C., Li, F. W., Yang, B., 2023. C2SPoint: A classification-to-saliency network for point cloud saliency detection. *Computers & Graphics*, 115, 274–284.

Lozić, E., Štular, B., 2021. Documentation of Archaeology-Specific Workflow for Airborne LiDAR Data Processing. *Geosciences*, 11(1), 26.

Nadel, D., Bar-Oz, G., Avner, U., Boaretto, E., Malkinson, D., 2010. Walls, ramps and pits: the construction of the Samar Desert kites, southern Negev, Israel. *Antiquity*, 84(326), 976–992.

Nadel, D., Bar-Oz, G., Perevolotsky, A., Malkinson, D., 2024. The V-shaped desert kites and their contribution to the Timnian economy. *Journal of Arid Environments*, 220, 105120.

Nadel, D., Malkinson, D., Bar-Oz, G., Nachmias, A., Avner, U., Horwitz, L., Baharavand, D., Porat., N., 2021. *The gazelle’s dream: game drives of the Old and New Worlds*. Sydney University Press, chapter Small, sparse and effective: the Negev and Sinai kites, 253–304.

Nazari, H., 2024. A review to the Desert Kite: State of the Art! *Journal of Pars Arian Territories*, 1(1).

Risbøl, O., Eidshaug, J. S. P., Bjerck, H. B., Gran, M. M., Rantala, K. R., Tivoli, A. M., Zangrando, A. F. J., 2023. UAV LiDAR in coastal environments: Archaeological case studies from Tierra del Fuego, Argentina, and Vega, Norway. *Archaeological Prospection*, 30(4), 533–557.

Sylaiou, S., Tsifodimou, Z.-E., Evangelidis, K., Stamou, A., Tavantzis, I., Skondras, A., Stylianidis, E., 2025. Redefining Archaeological Research: Digital Tools, Challenges, and Integration in Advancing Methods. *Applied Sciences*, 15(5), 2495.

Toumazet, J.-P., Vautier, F., Roussel, E., Dousteyssier, B., 2017. Automatic detection of complex archaeological grazing structures using airborne laser scanning data. *Journal of Archaeological Science: Reports*, 12, 569–579.

Vinci, A., Todisco, F., Mannocchi, F., 2016. Calibration of manual measurements of rills using Terrestrial Laser Scanning. *CATENA*, 140, 164–168.

Vinci, G., Vanzani, F., Fontana, A., Campana, S., 2024. LiDAR Applications in Archaeology: A Systematic Review. *Archaeological Prospection*, 32(1), 81–101.

Wang, S., Hu, Q., Wang, S., Ai, M., Zhao, P., 2024. Archaeological site segmentation of ancient city walls based on deep learning and LiDAR remote sensing. *Journal of Cultural Heritage*, 66, 117–131.

Zheng, T., Chen, C., Yuan, J., Li, B., Ren, K., 2019. Pointcloud saliency maps. *Proceedings of the IEEE/CVF International Conference on Computer Vision (ICCV)*, 1598–1606.

Štular, B., Lozić, E., Eichert, S., 2021. Airborne LiDAR-Derived Digital Elevation Model for Archaeology. *Remote Sensing*, 13(9), 1855.